# Steering the longitudinal photoelectron momentum in the above-threshold ionization with two not-quite-collinear laser beams

Birger Böning [1,2] and Stephan Fritzsche [1,2,3,*]
[1]*Helmholtz-Institut Jena, D-07743 Jena, Germany*
[2]*GSI Helmholtzzentrum für Schwerionenforschung GmbH, D-64291 Darmstadt, Germany*
[3]*Theoretisch-Physikalisches Institut, Friedrich-Schiller-Universität Jena, D-07743 Jena, Germany*

(Received 8 August 2022; accepted 7 September 2022; published 3 October 2022)

Strong-field atomic processes, driven by long-wavelength laser beams, are known to be affected by magnetic forces. In such beams, the Lorentz force pushes the photoelectrons along the beam direction and prevents their rescattering or recombination with the parent ions. In high-order harmonic generation (HHG), therefore, the yield of energetic photons is markedly suppressed, rendering x-ray radiation sources from high harmonics so far impractical. To compensate these magnetic forces and to reenable HHG at long wavelengths, a setup of two not quite collinear beams has been suggested recently but not much analyzed beyond classical arguments and with respect to accessible laser parameters. Using the nondipole strong-field approximation, we here investigate when the longitudinal momentum of the photoelectrons vanishes and how this noncollinear setup explicitly depends on the wavelength and intensity of the driving beams. We also demonstrate that an *optimal* crossing angle $\delta_0$ between these beams always exists for which the fraction of the returning electrons is maximized. This rather simple steering of the longitudinal momentum will allow an efficient HHG with driving beams deep in the midinfrared.

DOI: 10.1103/PhysRevA.106.043102

## I. INTRODUCTION

During the past decades, the observation of atoms in strong laser fields helped understand not only the quantum dynamics on ultrashort timescales, but also led to the development of robust tabletop radiation sources at rather high photon energies. Indeed, the fundamental processes of above-threshold ionization (ATI), Refs. [1,2] and high-harmonic generation (HHG), Refs. [3,4] can nowadays be mastered accurately by just tailoring the parameters of the driving laser beams [5–11]. Electrons, which are released and accelerated in the laser field, can be steered back to their parent ions and give then rise to energetic photoelectrons in ATI or the emission of photons in HHG, respectively.

Today, HHG is routinely applied to generate coherent radiation with photon energies of tens of eV, or even more, by using near-infrared driving beams [12]. The tabletop design of these sources makes it desirable to extend the HHG process towards the x-ray regime [12,13] by just following the simple cutoff law $\hbar\omega_{\max} = I_p + 3.17U_p$, where $I_p$ denotes the ionization potential of the target atoms and $U_p \sim I\lambda^2$ the (so-called) ponderomotive energy in the driving beam. Since, from a classical viewpoint, the ponderomotive energy is proportional to the intensity $I$ and the (square of the) wavelength $\lambda$, it appears straightforward to obtain high-energetic harmonics by simply increasing the wavelength $\lambda$ and/or intensity $I$ of the beam [14]. Unfortunately, however, this argument quickly breaks down owing to the magnetic field, and which leads to a Lorentz force $F_z \sim I\lambda$ along the beam axis. This force pushes the electrons away from their parent ions and, thus, prevents the recombination as needed for HHG. In practice, an increase of the cutoff photon energy generally leads to a *decrease* in the radiation yield [15,16] and which renders the HHG process unattractive as a x-ray radiation source.

Various proposals have been suggested in the literature to circumvent this problem with the magnetic field in the electron-photon interaction [17–21] with many of them being quite challenging with regard to the setup of the beams and targets. A much simpler scheme was suggested by Pisanty *et al.* [22], who proposed a gas target in the focus of two noncollinear, circularly polarized and counter-rotating beams with identical wavelengths and intensities but with a small crossing angle $\delta$ [cf. Fig. 1(a)]. For this scheme, Pisanty and co-workers [22] argued that a forward ellipticity in the target region may counteract the magnetic Lorentz force, thus, bringing the electron back to the parent ion. If these arguments indeed apply, the HHG yield may increase by several orders of magnitude.

However, whereas Pisanty and co-workers provide some profound estimates for their proposal, little has been said so far how the crossing angle, wavelength, and intensity of the driving beams affect such a noncollinear HHG setup. Moreover, the laser-electron interaction was treated only in low-order approximation in the Hamiltonian to account for the (local forward) ellipticity of the combined fields. To incorporate the magnetic electron-photon interaction in a more complete fashion into theory, a nondipole strong-field approximation (SFA) should be applied for any thorough treatment of such a noncollinear beam geometry [23–25].

*s.fritzsche@gsi.de

 

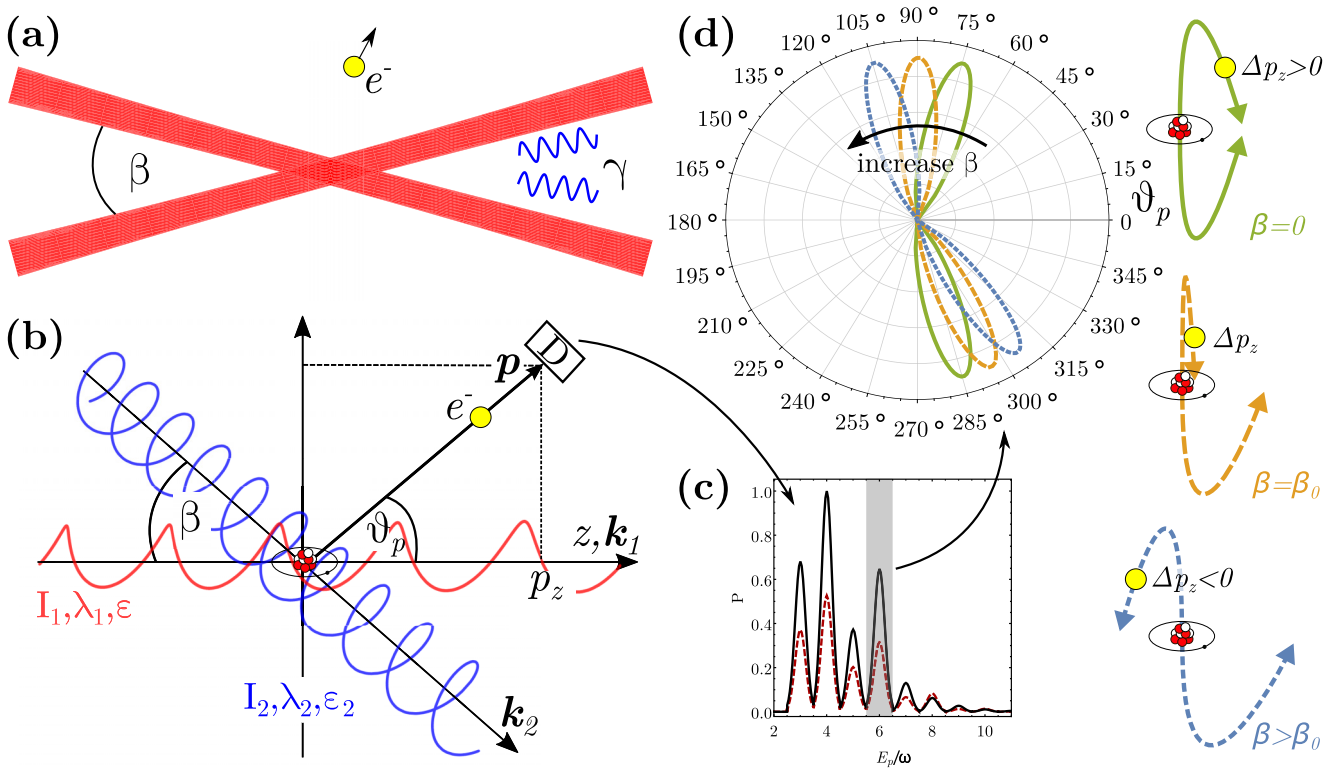


FIG. 1. Strong-field ionization by two not quite collinear laser beams. (a) If an atomic gas (green) is placed in the focus of two beams which propagate under the crossing angle $\delta$, electrons (yellow, ATI) or photons (blue, HHG) can both be emitted from the target gas cloud. (b) Detailed geometry of ATI as considered within the present theory: An atom is irradiated by two beams with intensities $I_1$, $I_2$, wavelengths $\lambda_1$, $\lambda_2$, and ellipticities $\epsilon_1$, $\epsilon_2$. A photoelectron with momentum $\boldsymbol{p} = (p, \vartheta_p, \varphi_p)$ is emitted in spherical coordinates and observed at the detector $D$. (c) The photoelectron energy spectra exhibit the well-known ATI peaks, spaced by the photon energy, whose magnitude varies with position and especially the polar angle $\vartheta_p$ of the detector. (d) A polar plot of the polar-angle distributions (PADs) readily reveals the role of the crossing angle $\delta$ and can be understood qualitatively by following the *classical* electron paths: For two collinear beams ($\delta = 0$, green solid line), the photoelectrons gain a longitudinal momentum $\Delta p_z$ along the beam axis owing to the Lorentz force and with two lobes tilted into the same direction. These lobes rotate counterclockwise if the crossing angle $\delta$ increases (orange dashed and blue dotted lines). For the *optimal* crossing angle $\delta = \delta_0$, half of the electrons (from the upper part of the PAD) will have the longitudinal momentum $\Delta p_z \approx 0$ (orange dashed line). For this optimal angle, half of the photoelectrons, therefore, remain on the $x$-$y$ reaction plane and return to their parent ions. This cancellation of the magnetic Lorentz force of the beams then enhances the yield of HHG photons or rescattered photoelectrons.

In this paper, we analyze and discuss the ATI process if driven by two not quite collinear laser beams with arbitrary wavelength, intensity, and ellipticity [cf. Fig. 1(b)]. By using our recently developed nondipole SFA [24], we show that the energy spectra and PAD of the photoelectrons strongly depend on the crossing angle $\delta$ of the beams [cf. Figs. 1(c) and 1(d)]. Especially, the PAD clearly reveal the magnetic Lorentz force which, for a single beam already, pushes the electrons away from the polarization plane $\vartheta_p = \pi/2$, leading to a nonzero and measurable forward momentum $\Delta p_z$ [26–28]. We here demonstrate that two noncollinear beams generally result into a counterclockwise rotation of the PAD and that an *optimal* crossing angle $\delta_0$ can be chosen between these beams for which the electrons from the upper half of the PAD (e.g., $\vartheta_p < \pi$) will remain within the polarization plane. This clearly increases the probability of these electrons to rescatter with their parent ions, especially when compared to a single driving beam, giving, thus, rise to a higher harmonic yield. Detailed computations show how $\delta_0$ depends on the wavelength and intensity of the driving beams and provide us with a *quantitative* guidance for generating high harmonics at long wavelengths. Much further work is, however, required to explicitly compute the harmonic yields by incorporating the *full* nondipole SFA amplitude for recombination into the time-dependent dipole moment of the target atoms. We use atomic units ($m_e = e = \hbar = 4\pi\varepsilon_0 = 1$) unless stated otherwise.

## II. THEORETICAL BACKGROUND

In order to apply the nondipole SFA [24] to the ionization by two not quite collinear laser beams, let us start from their combined field. We here assume that both beams can be approximated as monochromatic plane waves in Coulomb gauge [$\nabla \cdot \boldsymbol{A}(\boldsymbol{r}, t) = 0$] and that the combined electric and magnetic fields are just given by the sum of the vector potentials of the individual beams [29],

$$\begin{aligned} \boldsymbol{A}(\boldsymbol{r}, t) &= \boldsymbol{A}_1(\boldsymbol{r}, t) + \boldsymbol{A}_2(\boldsymbol{r}, t), \\ \boldsymbol{A}_j(\boldsymbol{r}, t) &= A_j^{(0)}[\cos(\boldsymbol{k}_j\boldsymbol{r} - \omega_j t)\, \boldsymbol{e}_{j,1} - \epsilon_j \sin(\boldsymbol{k}_j\boldsymbol{r} - \omega_j t)\boldsymbol{e}_{j,2}]. \end{aligned} \tag{1}$$

As usual, the amplitudes $A_j^{(0)} = \omega_j I_j^{1/2}(1+\epsilon_j^2)^{-1/2}$ of these vector potentials are defined by the intensities $I_j$, whereas $-1 \leqslant \epsilon_j \leqslant 1$ denote the ellipticities, $\omega_j = 2\pi c/\lambda_j$ denote the frequencies, and $\lambda_j$ denote the wavelengths. The wave-vectors $\boldsymbol{k}_j$ are chosen so that one of the beams propagates along the $z$ axis ($\boldsymbol{k}_1 = \omega_1/c\, \boldsymbol{e}_z$) and the second within the $x$-$z$ plane under the crossing angle $\delta$ with respect to the first beam [$\boldsymbol{k}_2 = \omega_2/c(-\sin\delta \boldsymbol{e}_x + \cos\delta \boldsymbol{e}_z)$]. For this geometry, the polarization planes of the two beams are defined by the unit vectors $\boldsymbol{e}_{1,1} = \boldsymbol{e}_x$, $\boldsymbol{e}_{1,2} = \boldsymbol{e}_y$, and $\boldsymbol{e}_{2,1} = \cos\delta \boldsymbol{e}_x - \sin\delta \boldsymbol{e}_z$, $\boldsymbol{e}_{2,2} = \boldsymbol{e}_y$, respectively. Whereas our nondipole SFA theory [24] covers rather general beam configurations, we will assume in this paper two counter-rotating and circularly polarized beams ($\epsilon_1 = -\epsilon_2 = 1$) with identical intensity $I = I_1 = I_2$ and wavelength $\lambda = \lambda_1 = \lambda_2$. We also assume two not quite collinear beams with a crossing angle $\delta \ll 1$. Whereas, in general, this analysis could be carried out also for rather arbitrary beam parameters, e.g., elliptically polarized beams or beams with different intensities $I_1 \neq I_2$, we here focus on the scenario that is best accessible, both theoretically and experimentally. Other beam configurations might indeed increase the ability to steer the momentum of the rescattered photoelectrons but are beyond the scope of the present paper.

For the sake of simplicity, moreover, we describe the target by a single atom in a (hydrogenike) $1s$ initial-state $|\Psi_0\rangle$, located within the focus of the beams at $z = 0$ [Fig. 1(b)], although our conclusions below will be valid for all atoms in the overlap region of the beams. Following Refs. [24,25], we will first compute the photoelectron momentum distribution by means of the SFA transition amplitude $T(\boldsymbol{p})$ and which formally excites an electron from its initial ground-state $|\Psi_0\rangle$ into the *nondipole* Volkov states $|\chi_{\boldsymbol{p}}(t)\rangle$. These continuum solutions include all magnetic corrections up to order $p/m_e c$ and are characterized by the asymptotic momentum $\boldsymbol{p} = (p, \vartheta_p, \varphi_p)$ of the photoelectrons at the detector [24]. For the vector potential (1), these nondipole Volkov states can be expressed in terms of plane waves as

$$\chi_{\boldsymbol{p}}(\boldsymbol{r}, t) = \frac{1}{(2\pi)^{3/2}} \sum_{N_1,N_2=-\infty}^{\infty} C_N(\boldsymbol{p}) e^{-i(E_N t - \boldsymbol{p}_N \boldsymbol{r})}, \qquad (2)$$

and where we have introduced the short-hand notation $N = (N_1, N_2)$. The expansion coefficients $C_N(\boldsymbol{p})$ depend on the photoelectron momentum $\boldsymbol{p}$ as well as the beam parameters $I$, $\lambda$, and $\delta$, which together determine the vector potential. The energies and momenta of the individual plane waves,

$$E_N = E_p + 2\,\tilde{U}_p - (N_1 + N_2)\omega,$$
$$\boldsymbol{p}_N = \boldsymbol{p} + \frac{2\tilde{U}_p p_z}{c\omega}\boldsymbol{k} - (N_1 + N_2)\boldsymbol{k},$$

can be given explicitly in terms of the photoelectron energy $E_p = p^2/2$ at the detector as well as the corrected ponderomotive energy $\tilde{U}_p = U_p/[1 - (p_z/c)^2]$. Since all the $\boldsymbol{k}_2$ and the coefficients $C_N$ depend on $\delta$, we, therefore, expect that the photoelectron momentum can be controlled to a good extent by just choosing the crossing angle between the beams.

With the expansion (2), the angle- and energy-differential ionization probability $\mathbb{P}(\boldsymbol{p}) = p|T(\boldsymbol{p})|^2$ can be readily expressed in terms of the direct SFA transition amplitude [24],

$$T(\boldsymbol{p}) = -i \int_{-\infty}^{\infty} dt\, \langle \chi_{\boldsymbol{p}}(t)|\hat{V}_{le}(\boldsymbol{r}, t)|\Psi_0(t)\rangle$$
$$= -2\pi i \sum_{N_1,N_2=-\infty}^{\infty} C_N(\boldsymbol{p}) V(\boldsymbol{p}_N)\delta(E_N + I_p), \qquad (3)$$

where the $\delta$ function designates the positions of discrete ATI peaks in the energy spectrum [cf. Fig. 1(c)]. The relative amplitudes of this spectrum are determined by the coefficients $C_N(\boldsymbol{p})$ and the matrix element $V(\boldsymbol{p}) = \langle \boldsymbol{p}|V(r)|\Psi_0\rangle$ of the atomic (Coulomb) potential $V(r)$. Owing to the geometry of the beams, we will restrict our analysis to photoelectrons that are emitted within the $p_x$-$p_z$ plane, i.e., for the azimuthal angle $\varphi_p = 0$. Figure 1(d) then displays the angular distributions $\mathbb{P}(\boldsymbol{p})$ as a function of the polar angle $\vartheta_p$ and for a fixed photoelectron energy $E_p = p^2/2$ but for selected crossing angles $\delta$.

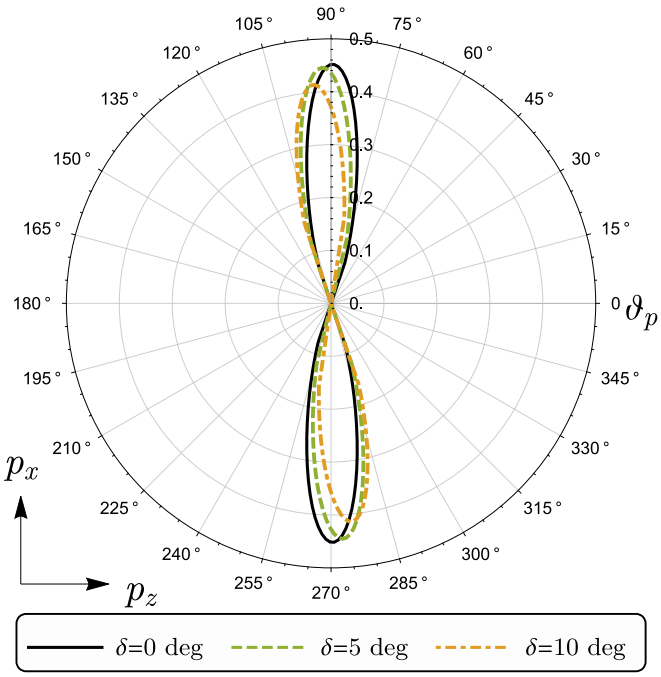


FIG. 2. PAD of photoelectrons with energy $E_p = 7.8$ eV $\approx 5\,\omega$ as emitted in the ATI with two not quite collinear laser beams ($I = 10^{14}$ W/cm$^2$, $\lambda = 800$ nm). Distributions on the $p_x$-$p_z$ plane ($\varphi_p = 0$) are shown for three values of the crossing angle $\delta = 0°$, $5°$, and $10°$ and for a neon target (ionization potential $I_p = 21.56$ eV).

## III. RESULTS AND DISCUSSION

Let us start with a neon target with ionization potential $I_p = 21.56$ eV. For such a target with tightly bound $2p$ valence electrons, Fig. 2 displays the computed angular distributions of ATI photoelectrons with energy $E_p = 7.8$ eV $\approx 5\,\omega$. As seen from the black solid curve in this figure, the PAD exhibits two lobes that, at first glance, are centered around the polarization plane ($\vartheta_p = \pi/2, 3\pi/2$) for co-propagating beams ($\delta = 0$). A closer inspection shows, however, that the maxima of the two lobes are slightly displaced from each other by $\vartheta_{p,\max} \neq \pi/2$

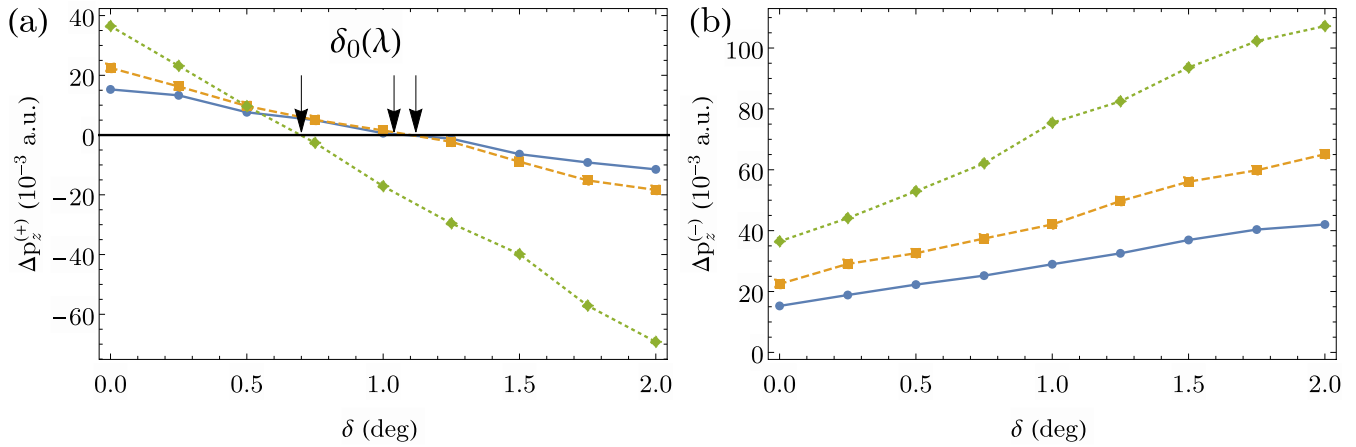


FIG. 3. Peak shifts $\Delta p_z$ as function of the crossing angle $\delta$ for a neon target with ionization potential $I_p = 21.56$ eV. Results are shown for (a) the peak shifts $\Delta p_z^{(+)}$ in the upper and (b) $\Delta p_z^{(-)}$ in the lower halves of the PAD for which the ionization probabilities become maximum as well as for three selected wavelengths of the incident beams: $\lambda = 800$ nm (blue solid curves), 1600 nm (orange dashed curves), 3200 nm (green dotted curves). The left panel (a) also displays the *optimal* crossing angle $\delta_0$ for the three wavelengths for which the peak shift $\Delta p_z^{(+)}$ in the upper half of the PAD vanishes. The beam intensity was set to $I = 1.5 \times 10^{14}$ W/cm$^2$ in all these computations.

$(3\pi/2)$ owing to the small nonzero longitudinal momentum $\Delta p_z = \sqrt{2E_p}\cos\vartheta_{p,\max}$. This peak shift is known to increase with the intensity and wavelength [24,26,27,30,31] of the incident laser light, in line with the classical Lorentz force $F_z \sim I\lambda$. If, therefore, this peak shift becomes too large, the electron misses its parent ion as indicated in Fig. 1(d).

For two not quite collinear beams with crossing angle $\delta$, the associated PAD rotates counterclockwise, i.e., the maxima of the PAD move both to the left in the upper half ($\vartheta < \pi$) of the $x$-$z$ scattering plane and to the right in the lower half [cf. the green dashed and orange dot-dashed curves in Fig. 2]. Or, equivalently, the peak shift $\Delta p_z^{(+)}$ decreases for all electrons that are emitted in the upper half, whereas their shift $\Delta p_z^{(-)}$ increases in the lower half. In practice, therefore, only half of the released electrons are driven back towards the polarization plane and, hence, their target ions, whereas the other half is accelerated even further away owing to the total Lorentz force [cf. Fig. 1(d)]. Whereas this behavior is strictly true only for directly emitted photoelectrons, our discussion is relevant also for those electrons that are driven back to the parent ion, instead of being measured at the detector. Indeed, this rotation of the PAD has been found quite *universal* in the non-dipole SFA above for all photoelectron energies that contribute significantly to the ATI spectra and, thus, confirm the classical arguments by Pisanty and co-workers [22]. For a proper choice of the crossing angle $\delta$ of the two beams, we, therefore, expect overall that the (upper) half of the photoelectrons will be steered back to their ions. Figure 3 displays the peak shifts $\Delta p_z^{(+)}$ and $\Delta p_z^{(-)}$ as functions of the crossing angle $\delta$ for a neon target with ionization potential $I_p = 21.56$ eV and for beams of given wavelength and intensity. Results are shown especially for beams with intensity $I = 1.5 \times 10^{14}$ W/cm$^2$ and the three wavelengths $\lambda = 800$ nm (blue solid curves), 1600 nm (orange dashed curves), and 3200 nm (green dotted curves), respectively. For all these beam parameters, an *optimal* crossing angle $\delta_0$ *does* exist, for which (half of) the emitted electrons return to their parent ions [cf. Fig. 1(d)] and may enhance their rescattering or recombination with the parent ions.

Figure 3 can be readily understood in terms of the (classical) Lorentz force that acts upon all charges in motion. For two co-propagating beams with $\delta = 0$, for instance, the (magnetic) force components of the two beams simply add to each other and scales linearly with the wavelength ($F_z \sim I\lambda$). For $\delta = 0$, therefore, the peak shifts $\Delta p_z^{(+)} = \Delta p_z^{(-)}$ increase as the wavelength is enlarged. These simple arguments also agree with a classical analysis in which the (cycle-averaged) magnetic Lorentz force $F_z = \langle[\boldsymbol{v} \times \mathcal{B}]_z\rangle = [1 - f(\delta)]I\lambda$ with an always positive function $f(\delta)$, just depends on the initial conditions (i.e., the emission into the upper or lower half of the PAD) but neither on the intensity $I$ nor the wavelength $\lambda$. In our (quantum-mechanical) nondipole theory for the direct amplitude, this shift is encoded into the wavelength dependence of the expansion coefficients $C_N(\boldsymbol{p})$, and which then enter the nondipole Volkov states (2). As seen from Fig. 3, moreover, the influence of the Lorentz forces, e.g., the slope of the curves, decreases with increasing laser frequencies.

Most important, perhaps, and as readily seen from Fig. 3(a), such an *optimal* crossing angle $\delta_0$ can be found for any wavelength $\lambda$. Whereas Fig. 3 itself displays only peak shifts for those electrons, which propagate directly to the detector, similar arguments apply also for the rescattering or recombination of electrons. This can be explained by just following their *classical* pathes [cf. Fig. 1(d)]: If $\delta = 0$, the electron will be pushed away from its parent ion for all directions of initial emission, whereas for $\delta = \delta_0$, the electron returns to its parent ion if it has been emitted before with positive momentum along the $x$ axis. For $\delta > \delta_0$, in contrast, the sign of the longitudinal momentum is changed and the electron will miss its parent ion again.

With this quite general behavior in mind, the noncollinear setup of laser beams in Fig. 1(a) can be applied to counteract the Lorentz force and to enhance the recombination or rescattering of electrons by the parent ions. For an optimally chosen crossing angle $\delta_0$, this may enlarge also the yield of high

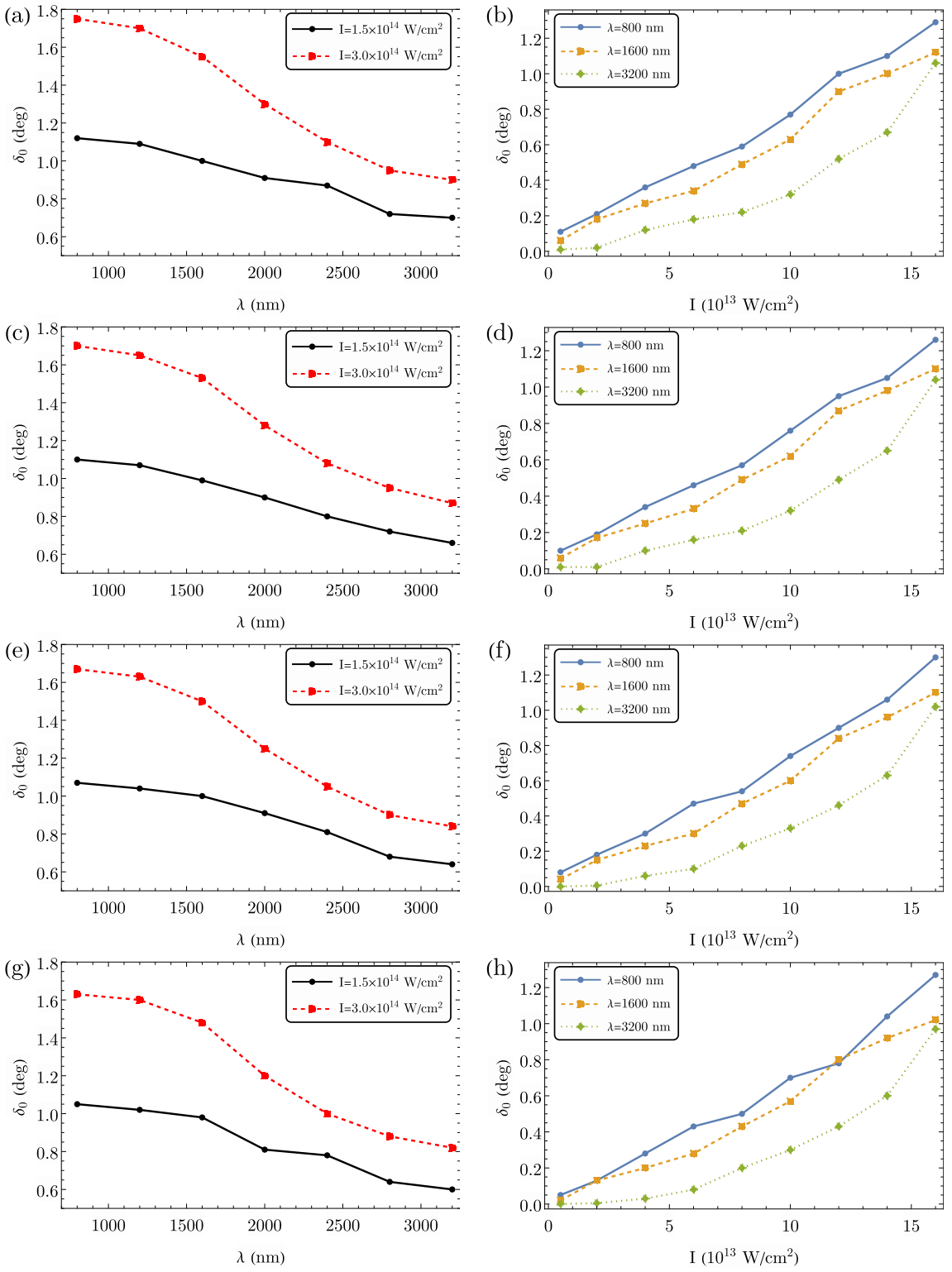


FIG. 4. Optimal crossing angle $\delta_0$ as function of wavelength $\lambda$ (left panels) and intensity $I$ of the laser pulses (right panels). Results are shown for the four noble gases neon [(a) and (b) $I_p = 21.56$ eV], argon [(c) and (d) $I_p = 15.76$ eV], krypton [(e) and (f)$I_p = 14.00$ eV], and xenon [(g) and (h) $I_p = 12.13$ eV], respectively. Moreover, all these calculations were performed within the long-wavelength regime for the two intensities $I = 1.5 \times 10^{14}$ W/cm$^2$ (black solid lines) and $I = 3.0 \times 10^{14}$ W/cm$^2$ [red dashed lines; (a), (c), (e), and (g)] and the three wavelengths $\lambda = 800$ nm (blue solid lines), $\lambda = 1600$ nm (orange dashed lines), and $\lambda = 3200$ nm [olive dotted lines; (b), (d), (f), and (h)]. At the optimal crossing angle $\delta_0$, the peak shift vanishes for the electrons in the upper half ($\Delta p_z^{(+)} = 0$) and helps them return to their parent ions within the polarization plane.

harmonics or the nonsequential double ionization in strong laser fields. To further understand how such an enhancement depends on the laser parameters, the left panels of Fig. 4 display the optimal crossing angle $\delta_0$ as the function of wavelength $\lambda$ and for the four noble gases neon, argon, krypton, and xenon, respectively. These optimal angles are shown for two intensities $I = 1.5 \times 10^{14}$ W/cm$^2$ (black solid lines) and $I = 3.0 \times 10^{14}$ W/cm$^2$ (red dashed lines). By starting from the widely used 800 nm of Ti-sapphire lasers for HHG and by going towards midinfrared lasers, the angular $\delta_0$ decreases for all intensities and then requires their fine-tuning within about $0.1^\circ$ in order to ensure the return of electrons, well of what appears experimentally feasible today [32]. This dependence was shown in Ref. [24] and just reflects the increasing peak shift for identical laser parameters if the ionization potential increases. On the right panels of Fig. 4, this optimal angles are displayed as function of the intensity and for three selected wavelengths: $\lambda = 800$ nm (blue solid lines), $\lambda = 1600$ nm (orange dashed lines), and $\lambda = 3200$ nm (olive dotted lines). The increase in$\delta_0$ with intensity here follows from the proportionality between the Lorentz force and intensity and, hence, a larger angle $\delta$ for the compensation of this force. This dependence of the optimal angle $\delta_0$ on the wavelength and intensity of the noncollinear beams, presented in Fig. 4, also constitute the major result of this paper.

Large angles $\delta_0$ arise indeed only for rather high intensities of the driving beams [cf. Fig. 4(b)]. At the first glance, this behavior of $\delta_0$ as function of the laser wavelength and intensity may appear *counterintuitive* since the cycle-averaged Lorentz force $F_z \sim I\lambda$ just obeys the same dependence on both parameters. In practice, however, the full Lorentz force also contains a $z$-dependent factor that arises from the perodicity of the fields and, hence, depends on the wavelength but not the intensity of the laser pulses. This is often discussed in terms of the $\lambda$-dependent (oscillating) *figure-eight* motion of electrons in the laser field, that occurs in addition to their (classical) drift, owing to the the cycle-averaged Lorentz force. Whereas a more detailed analysis of the *classical* dynamics of the photoelectron in such a crossed-beam scenarios will be very interesting, this is beyond the scope of the present paper.

Whereas the (magnitude of) peak shifts of the direct photoelectrons certainly provide guidance for choosing the laser parameters and for a possible enhancement of the high-harmonic yields, further experimental and theoretical work will be needed for realizing such a noncollinear excitation scheme successfully. We especially expect the experimental setup to be realized in a straightforward fashion, whereas the nondipole theory still need to be extended for the rescattering and/or recombination amplitudes. This extension appears feasible to us but requires the calculation of the time-dependent harmonic dipole moment of the active electron [33]. A preliminary estimate on this dipole moment was obtained in Ref. [22] and suggests at $\lambda = 800$ nm an increase by about two orders of magnitude in the harmonic yield when two not quite collinear beams with a crossing angle $\delta = 2^\circ$ are compared with a single beam of equal intensity. This implies a quite similar trend as found for the direct ATI photoelectrons in the present paper and help justify our approach here. With a full treatment of the nondipole Volkov states (2) in the evaluation of the dipole moment, we, however, expect more reliable predictions for the harmonic yield as a function of $\delta$ as well as for other features of the harmonic energy spectra.

Our findings above demonstrate that a noncollinear beam setup might indeed be a very powerful tool for compensating the longitudinal momentum of photoelectrons in ATI experiments. It facilitates to drive the electrons back to their parent ions and to enhance the high-harmonic yield, if the intensity and wavelength are properly tuned towards a large cutoff energy $\hbar\omega = I_p + 3.17U_p$.

## IV. SUMMARY AND CONCLUSIONS

To summarize, we have demonstrated in this paper how two not quite collinear and counter-rotating laser beams help cancel the magnetic Lorentz forces that act upon the photoelectrons in strong-field ATI experiments. By applying our recently developed nondipole SFA, we are able to explained the cancellation of the longitudinal momentum for roughly half of the emitted electrons. Indeed, this fraction of emitted electrons remain in the polarization plane and are, hence, driven back to their parent ions. This noncollinear setup of laser beams can, therefore, be applied also for driving HHG at long wavelengths and high intensities and for which the yield is typically strongly suppressed.

We also validate that an optimal crossing angle $\delta_0$ can always be found for two noncollinear driving beams and for maximizing the fraction of returning electrons. The dependence of this angle $\delta_0$ with regard to the wavelength and intensity of the driving beams is evaluated for a good range of laser parameters, and this confirms that the associated setup appears experimentally to be feasible. We, therefore, expect such experiments to be soon performed and analyzed for its use in HHG at long wavelengths. In the future, further theoretical work is needed in order to explicitly compute the yields of harmonic radiation within the nondipole theory by including the structure of both, the laser pulse and target atoms [34–36]. Such a potential in the harmonic yield is of great interest for many applications.

## ACKNOWLEDGMENTS

This work has been funded by the Deutsche Forschungsgemeinschaft (DFG, German Research Foundation) under Project No. 440556973.

[1] P. Agostini, F. Fabre, G. Mainfray, G. Petite, and N. K. Rahman, Phys. Rev. Lett. **42**, 1127 (1979).

[2] G. G. Paulus, W. Nicklich, H. Xu, P. Lambropoulos, and H. Walther, Phys. Rev. Lett. **72**, 2851 (1994).

[3] A. McPherson, G. Gibson, H. Jara, U. Johann, T. S. Luk, I. A. McIntyre, K. Boyer, and C. K. Rhodes, J. Opt. Soc. Am. B **4**, 595 (1987).

[4] M. Ferray, A. L'Huillier, X. F. Li, L. A. Lompre, G. Mainfray, and C. Manus, J. Phys. B: At., Mol. Opt. Phys. **21**, L31 (1988).

[5] P. B. Corkum and F. Krausz, Nat. Phys. **3**, 381 (2007).

[6] W. Paufler, B. Böning, and S. Fritzsche, Phys. Rev. A **98**, 011401(R) (2018).

[7] K. M. Dorney, L. Rego, N. J. Brooks, J. San Román, C.-T. Liao, J. L. Ellis, D. Zusin, C. Gentry, Q. L. Nguyen, J. M. Shaw, A. Picón, L. Plaja, H. C. Kapteyn, M. M. Murnane, and C. Hernández-García, Nat. Photonics **13**, 123 (2019).

[8] B. Böning, W. Paufler, and S. Fritzsche, Phys. Rev. A **98**, 023407 (2018).

[9] W. Paufler, B. Böning, and S. Fritzsche, Phys. Rev. A **100**, 013422 (2019).

[10] D. B. Milošević and W. Becker, Phys. Rev. A **102**, 023107 (2020).

[11] N. Eicke, S. Brennecke, and M. Lein, Phys. Rev. Lett. **124**, 043202 (2020).

[12] M. Kohler, T. Pfeifer, K. Hatsagortsyan, and C. Keitel, *Advances In Atomic, Molecular, and Optical Physics* (Elsevier, Amsterdam, 2012), pp. 159–208.

[13] T. Popmintchev, M.-C. Chen, D. Popmintchev, P. Arpin, S. Brown, S. Alisauskas, G. Andriukaitis, T. Balciunas, O. D. Mucke, A. Pugzlys, A. Baltuska, B. Shim, S. E. Schrauth, A. Gaeta, C. Hernandez-Garcia, L. Plaja, A. Becker, A. Jaron-Becker, M. M. Murnane, and H. C. Kapteyn, Science **336**, 1287 (2012).

[14] C. Hernández-García, J. A. Pérez-Hernández, T. Popmintchev, M. M. Murnane, H. C. Kapteyn, A. Jaron-Becker, A. Becker, and L. Plaja, Phys. Rev. Lett. **111**, 033002 (2013).

[15] N. J. Kylstra, R. M. Potvliege, and C. J. Joachain, J. Phys. B: At., Mol. Opt. Phys. **34**, L55 (2001).

[16] A. S. Emelina, M. Y. Emelin, and M. Y. Ryabikin, Quantum Electron. **44**, 470 (2014).

[17] R. Fischer, M. Lein, and C. H. Keitel, Phys. Rev. Lett. **97**, 143901 (2006).

[18] M. Verschl and C. H. Keitel, Europhys. Lett. **77**, 64004 (2007).

[19] M. Klaiber, K. Z. Hatsagortsyan, C. Müller, and C. H. Keitel, Opt. Lett. **33**, 411 (2008).

[20] H. K. Avetissian, A. G. Markossian, and G. F. Mkrtchian, Phys. Rev. A **84**, 013418 (2011).

[21] M. C. Kohler and K. Z. Hatsagortsyan, Phys. Rev. A **85**, 023819 (2012).

[22] E. Pisanty, D. D. Hickstein, B. R. Galloway, C. G. Durfee, H. C. Kapteyn, M. M. Murnane, and M. Ivanov, New J. Phys. **20**, 053036 (2018).

[23] L. Rosenberg and F. Zhou, Phys. Rev. A **47**, 2146 (1993).

[24] B. Böning, W. Paufler, and S. Fritzsche, Phys. Rev. A **99**, 053404 (2019).

[25] B. Böning, W. Paufler, and S. Fritzsche, Phys. Rev. A **101**, 031401(R) (2020).

[26] C. T. L. Smeenk, L. Arissian, B. Zhou, A. Mysyrowicz, D. M. Villeneuve, A. Staudte, and P. B. Corkum, Phys. Rev. Lett. **106**, 193002 (2011).

[27] A. Ludwig, J. Maurer, B. W. Mayer, C. R. Phillips, L. Gallmann, and U. Keller, Phys. Rev. Lett. **113**, 243001 (2014).

[28] J. Maurer, B. Willenberg, J. Daněk, B. W. Mayer, C. R. Phillips, L. Gallmann, M. Klaiber, K. Z. Hatsagortsyan, C. H. Keitel, and U. Keller, Phys. Rev. A **97**, 013404 (2018).

[29] S. Fritzsche and B. Böning, Phys. Rev. Res. **4**, 033031 (2022).

[30] B. Wolter, M. G. Pullen, M. Baudisch, M. Sclafani, M. Hemmer, A. Senftleben, C. D. Schröter, J. Ullrich, R. Moshammer, and J. Biegert, Phys. Rev. X **5**, 021034 (2015).

[31] J. Daněk, M. Klaiber, K. Z. Hatsagortsyan, C. H. Keitel, B. Willenberg, J. Maurer, B. W. Mayer, C. R. Phillips, L. Gallmann, and U. Keller, J. Phys. B: At., Mol. Opt. Phys. **51**, 114001 (2018).

[32] D. D. Hickstein, F. J. Dollar, P. Grychtol, J. L. Ellis, R. Knut, C. Hernández-García, D. Zusin, C. Gentry, J. M. Shaw, T. Fan, K. M. Dorney, A. Becker, A. Jaroń-Becker, H. C. Kapteyn, M. M. Murnane, and C. G. Durfee, Nat. Photonics **9**, 743 (2015).

[33] K. Amini, J. Biegert, F. Calegari, A. Chacón, M. F. Ciappina, A. Dauphin, D. K. Efimov, C. F. de Morisson Faria, K. Giergiel, P. Gniewek, A. S. Landsman, M. Lesiuk, M. Mandrysz, A. S. Maxwell, R. Moszyński, L. Ortmann, J. A. Pérez-Hernández, A. Picón, E. Pisanty, J. Prauzner-Bechcicki *et al.*, Rep. Prog. Phys. **82**, 116001 (2019).

[34] D. B. Milošević, Phys. Rev. A **92**, 043827 (2015).

[35] S. Fritzsche, Comput. Phys. Commun. **240**, 1 (2019).

[36] B. Böning and S. Fritzsche, Phys. Rev. A **102**, 053108 (2020).